

Comparing extragalactic megahertz-peaked spectrum and gigahertz-peaked spectrum sources

F.J. Ballieux¹, J.R. Callingham^{2,1}, H.J.A. Röttgering¹, and M.M. Slob¹

¹ Leiden Observatory, Leiden University, PO Box 9513, 2300 RA Leiden, The Netherlands
 e-mail: ballieux@strw.leidenuniv.nl

² ASTRON, Netherlands Institute for Radio Astronomy, Oude Hoogeveensedijk 4, Dwingeloo 7991 PD, The Netherlands

Received ; accepted

ABSTRACT

Sensitive wide-field radio surveys, such as the LOFAR Two Meter Sky Survey (LoTSS), the LOFAR LBA Sky Survey (LoLSS), and the Very Large Array Sky Survey (VLASS), now enable the selection of statistically large samples of peaked-spectrum (PS) sources. PS sources are compact radio sources with a peak in their radio continuum spectrum. They are considered the precursors to standard FRI and FRII radio galaxies.

We present a sample of 8,539 gigahertz-peaked spectrum (GPS) sources with spectral turnovers near 1400 MHz, and a sample of 508 megahertz-peaked spectrum (MPS) sources with turnovers near 144 MHz. Our MPS sample is the largest sample of MPS sources identified to date by a factor of 1.4. Our GPS sample is almost six times larger than any previously known sample of PS sources. These large sample sizes allow a robust comparison between GPS sources and MPS sources, allowing us to investigate the differences between these types of sources and study their lifetimes.

The Euclidean normalized source counts of both samples match the shape of the general radio-loud active galactic nuclei (AGN) samples, scaled down by a factor ~ 45 for the MPS sample, and a factor ~ 29 for the GPS sample. Assuming no cosmological evolution, these offsets imply that both MPS and GPS sources have shorter lifetimes than general AGN, with MPS sources tending to have significantly shorter lifetimes compared to GPS sources. This offset could be explained through simulations of PS sources, which show that GPS sources traverse through the surrounding medium with lower speed than MPS sources, causing MPS sources to have shorter lifetimes.

Aside from sample statistics, we also identify a clearly restarted radio source that has a peaked-spectrum core surrounded by large radio lobes. Furthermore, we identify four sources that are extremely steep-spectrum below their turnover, implying this turnover must be associated with Free-Free Absorption, which would imply these sources are surrounded by a dense medium.

Key words. galaxies: active – galaxies: evolution – radio continuum: galaxies – galaxies: statistics

1. Introduction

Peaked-spectrum (PS) sources are compact sources that show a peak in their radio spectrum and have been hypothesized to be the young progenitors of radio-loud AGN. These sources can be found with a range of intrinsic turnover frequencies $\nu_{\text{rest,turn}}$. PS sources are typically classified into the sub-classes: gigahertz-peaked spectrum (GPS) sources, high-frequency peaked (HFP) sources, compact steep-spectrum (CSS) sources, and megahertz-peaked-spectrum (MPS) sources. These sub-classes differ in terms of linear size and turnover frequency, but are likely part of the continuum of radio galaxies, with HFP sources the smallest and MPS sources the largest. A correlation between the projected linear size l in kpc, and the turnover frequency in GHz of these sources has been identified by O'Dea (1998) and is given by $\nu_{\text{rest,turn}} \propto l^{-0.65}$. Small PS sources thus have higher turnover frequencies.

HFP sources are sources with a spectral turnover above 5 GHz (O'Dea & Saikia 2021), and are the most compact PS sources (Dallacasa et al. 2001). GPS radio sources have spectral peaks between 500 MHz and 5 GHz (Gopal-Krishna et al. 1983). They have typical linear sizes $\lesssim 1$ kpc, and are powerful, with $\log P_{1.4\text{GHz}} \gtrsim 25\text{WHz}^{-1}$ (O'Dea 1998). CSS sources are just as powerful as GPS sources, with larger linear sizes (1–20 kpc; Fanti et al. 1990), and spectral peaks at < 500 MHz.

MPS sources are sources that peak below 1 GHz in the observer's frame. The MPS population is likely to be a combination of relatively nearby CSS and GPS sources, or compact high-frequency peaked sources further away, whose turnover frequency has been shifted to low frequencies due to the cosmological redshift (O'Dea & Saikia 2021).

There are two main hypotheses as to what produces the spectral turnovers and small linear sizes of PS sources. One of these hypotheses is that PS sources are the young precursors of Fanaroff-Riley I and II (FRI and FRII) galaxies. PS sources often show evidence of compact double-lobed structures (O'Dea 1998). Furthermore, a relationship between radio power and linear size has been found for PS sources (e.g. Kunert-Bajraszewska et al. 2010, An & Baan 2012). From the relation between linear size and turnover frequency, we find that if the youth model applies the majority of the time, we would expect HFP sources to be the youngest PS sources, evolving into GPS sources, then into MPS sources, and finally into FRI and FRII sources. (e.g. Carvalho 1985, Kunert-Bajraszewska et al. 2010). Evidence from spectral break modeling (Callingham et al. 2015) and the motions of lobe hot spots (Owsianik & Conway 1998, Kaiser & Best 2007) supports this theory. In the youth hypothesis, synchrotron self-absorption (SSA; Snellen et al. 2000, de Vries et al. 2009) is the cause of the spectral turnover.

The other hypothesis is that the small linear sizes and spectral turnovers of PS sources are caused by their radio jets being contained within dense circumnuclear environments. Due to the dense environments, sources get 'frustrated', and they are not able to grow to larger spatial scales. The absorption mechanism associated with the frustration hypothesis is Free-Free Absorption (FFA; Bicknell et al. 1997, Peck 1999, Callingham et al. 2015). Evidence for the frustration hypothesis is that the radio morphologies of CSS sources indicate strong interactions between the jets of a source and their environments (Wilkinson et al. 1984, van Breugel et al. 1984, Kunert-Bajraszewska et al. 2010). Furthermore, extended emission around PS sources has been observed, indicating multiple epochs of activity (Baum et al. 1990, Stanghellini et al. 1990). In individual PS sources, unusually high densities have been found, which also indicates FFA emission would be dominant (Peck 1999, Callingham et al. 2015, Sobolewska et al. 2019).

Generally, it is assumed that the majority of PS sources are young rather than frustrated (O'Dea & Saikia 2021). It is always possible that a source is both young and frustrated, and individual PS sources could be associated with either or both mechanisms. In this work, we will assume that the youth hypothesis is dominant over the frustration hypothesis.

Most research that has been done on PS sources in the last years (e.g. Snellen et al. 1998; Callingham et al. 2017; Slob et al. 2022) has focused on determining the cause of the spectral turnovers and the small linear sizes of PS sources. None of these studies have compared the different types of PS sources against each other, which is vital in determining the evolution of sources from HFP sources all the way to FRI and FRII sources. By studying the abundances of the different types of PS sources, we can determine the relative lifetimes of these phases and understand how the population of large-scale radio sources has evolved over time. Such an analysis requires statistically large samples of MPS, GPS, and HFP sources.

In the past decades, a revolution has taken place in wide-field radio astronomy. Surveys of unparalleled sensitivity, resolution, and sky area have been made. In this work, we will make use of all-sky surveys from the LOw Frequency ARray (LOFAR; van Haarlem et al. 2013) and the Karl G. Jansky Very Large Array (VLA). From LOFAR, we use the LOFAR Two-meter Sky Survey (LoTSS; Shimwell et al. 2022) and the LOFAR LBA Sky Survey (LoLSS; de Gasperin et al. 2023). Using these surveys, we are able to determine the low-frequency part of the spectral energy distribution (SED) of more sources than ever before. Constraining the low-frequency region of SEDs is vital in determining spectral turnovers and thus identifying PS sources, specifically MPS sources with lower-frequency turnovers. The Very Large Array Sky Survey (VLASS; Lacy et al. 2020), which is a higher frequency survey, allows us to extend this research to GPS sources with turnovers at higher frequencies. Now that such surveys are available, we can construct larger samples of MPS and GPS sources than ever before, and we can compare these samples with each other. From these samples we can find the relative abundances of these sources in the radio sky, and determine their relative lifetimes, with statistical robustness.

The surveys used in this work will be further introduced in Section 2. They allow us to compile master samples of unresolved isolated radio sources, as will be described in Section 3. In Section 4, we use these master samples to identify samples of MPS and GPS sources larger and more complete than ever before. In Section 5 we construct Euclidean normalized source counts for our PS samples, which helps us understand the abun-

dances of PS sources in the radio sky and allows us to draw conclusions about their relative lifetimes.

In this paper we adopt $H_0 = 70 \text{ km s}^{-1} \text{ Mpc}^{-1}$, $\Omega_M = 0.27$ and $\Omega_\Lambda = 0.73$ for a standard Lambda cold dark matter cosmological model (Hinshaw et al. 2013).

2. Surveys

To select our samples of PS sources, we used LoLSS, LoTSS, VLASS, and the NRAO VLA Sky Survey (NVSS; Condon et al. 1998). These surveys are among the most sensitive wide-field radio surveys to date, which has allowed us to select the faintest PS sources. The sensitivity of common wide-field radio surveys is illustrated in Figure 1. We indicate the lowest reported flux density for many wide-field radio surveys from the last three decades. We also plot the faintest typical SSA PS sources that could be observed in the PS samples from Slob et al. (2022) and Callingham et al. (2017), as well as the faintest PS samples that could be observed in our GPS and MPS samples. We find that our MPS sample reaches almost four times lower flux densities than Slob et al. (2022), and our GPS sample reaches an over 40 times lower flux density than Callingham et al. (2017).

We can determine from Figure 1 that the sensitivity of LoLSS limits the faintest MPS sources we can identify, while the sensitivity of NVSS limits the faintest GPS sources selected.

2.1. LOFAR surveys

LOFAR (van Haarlem et al. 2013) consists of 52 stations centered in the Netherlands. The stations consist of high-band (HBA, 110–250 MHz) and low-band (LBA, 10–90 MHz) antennae.

LoTSS (Shimwell et al. 2022) is a deep wide-field radio survey, performed with the LOFAR HBA at 120–168 MHz. It aims to observe the whole northern sky. Data from the second data release (DR2) was used in this work, which consists of observations from 27 % of the northern sky. The coverage is split into two regions centered at approximately 12h45m+44° 30' and 1h00m+2° 00', spanning 4178 deg² and 1457 deg², respectively. The DR2 catalog contains 4,396,228 radio sources, derived from the total intensity maps. It reaches a median rms sensitivity of 83 μJy beam⁻¹, a resolution of 6'', and is 90 % complete at 0.8 mJy beam⁻¹.

In-band spectra are also available for the sources in LoTSS, at central frequencies 128, 144, and 160 MHz. The in-band spectra provide information about spectral properties along the 48 MHz wide band. However, these in-band spectra are not reliable for most sources, due to the narrow frequency range, combined with non-negligible uncertainties in the alignment of the flux density scale of the in-band images. Therefore, the in-band spectra were only used in this work as a visual guide to confirm spectral fits and were not used to select PS sources.

LoLSS (de Gasperin et al. 2023) is a LOFAR wide-area survey at 42–66 MHz, centered at 54 MHz, which eventually will cover the whole sky above a declination of 24°. In this work, data from the first data release (DR1) was used, which has a typical sensitivity of 1.55 mJy beam⁻¹, four times higher relative to the LoLSS preliminary data release (PDR; de Gasperin et al. 2021). So far, 650 deg² sky area has been released, centered around the Hobby-Eberly Telescope Dark Energy Experiment (HETDEX; Hill et al. 2008) Spring Field with 11 < RA < 16h and 45 < Dec < 62°. The LoLSS DR1 catalog consists of 42,463 sources, with an angular resolution of 15'', and 95% completeness at 11 mJy.

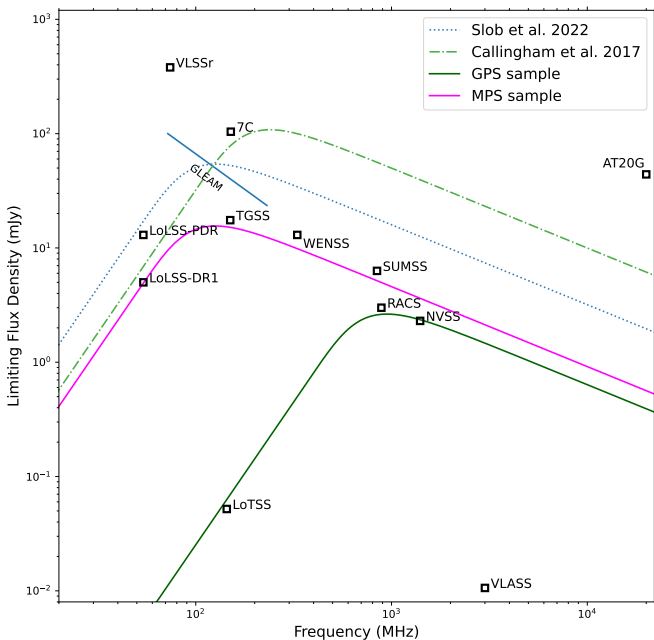


Fig. 1: The observational limits of different radio surveys and PS samples. The lowest cataloged component flux density reported for each survey used in this research, and other relevant large radio surveys, is indicated in the plot. The GaLactic and Extra-galactic All-Sky MWA Survey (GLEAM; Wayth et al. 2015) is represented by a line since it has variable limiting flux densities at different observing frequencies. The Callingham et al. (2017) sample is represented by an SSA model with a faintest peak flux density of 160 mJy at a turnover frequency of 190 MHz. The Slob et al. (2022) sample is represented by an SSA model with a faintest peak flux density 80 mJy at a turnover frequency of 100MHz. We indicate the observational limits of our MPS and GPS samples with SSA models with a limiting flux density of 23 mJy at a turnover frequency of 100 MHz, respectively 3.9 mJy at 750 MHz. It should be noted that these curves merely have an illustrative purpose. Since PS sources are identified by at least three flux density measurements at different frequencies, we cannot fit the exact turnover frequency. The sources in our sample have a wide range of possible turnover frequencies and corresponding flux densities. In this plot, we indicate the faintest PS sources that could theoretically be identified in our master samples, if the turnover frequency was approximately at the central radio survey of each sample. In the figure, multiple wide-field radio surveys were indicated that have not been mentioned before; Faint Images of the Radio Sky at Twenty-centimeters (FIRST; Becker et al. 1995), the Westerbork Northern Sky Survey (WENSS; Rengelink et al. 1997), Sydney University Molonglo Sky Survey (SUMSS; Mauch et al. 2003), Cambridge 7C (Hales et al. 2007), Australia Telescope 20 GHz (AT20G; Murphy et al. 2010), Very Large Array Low-Frequency Sky Survey Redux (VLSSr; Lane et al. 2014), TIFR GMRT Sky Survey Alternative Data Release 1 (TGSS; Intema et al. 2017), and the RAPID ASKAP Continuum Survey (RACS; Hale et al. 2021).

Separate in-band spectra, at central frequencies 44, 48, 52, 56, 60, and 64 MHz, are also available. The in-band spectra were only used for visual confirmation that spectral fits seem reliable, and were not used for selecting PS sources.

2.2. VLA surveys

NVSS (Condon et al. 1998) is a 1.4 GHz sky survey performed with the VLA, covering the sky north of a declination of -40° (82% of the celestial sphere). Observations were completed between September 1993 and October 1996. The NVSS catalog consists of 1,773,484 sources, has a resolution 45'', and is 99% complete at 3.4 mJy.

The Very Large Array Sky Survey (VLASS; Lacy et al. 2020) is a wide-field radio survey at 2-4 GHz, centered at 3 GHz, with an angular resolution of 2.5'', covering the whole sky above a declination of -40° ($33,885\text{deg}^2$). It has a 1σ goal of $70\mu\text{Jybeam}^{-1}$. The B configuration of the VLA was used, with a maximum antenna separation of 10km.

VLASS has observed the entire sky three times, which allows for studies of variable and transient sources. By the time of writing, the first and second epochs have been processed. Quick look (QL) images for the first two epochs have been released. The rapid CLEANing of these images limits the quality of these images, but they are reliable for our science since the majority of the VLASS sources we are interested in are high signal-to-noise point sources (Gordon 2023). In our research, the component catalog of epochs 2.1 and 2.2 was used. We only use the second epoch because the rapid CLEAN algorithm used was updated between epochs 1.1 and 1.2. There are a number of issues with epoch 1.1, key issues being a systematic under-measurement of flux density value in the QL images, issues with astrometry, and ghost images of bright sources. These issues have been solved for the second epoch, so we disregard epoch 1 (Gordon 2023). The VLASS QL catalog consists of 2,995,271 components.

3. Sample selection

In this work, we select two master samples, the low-frequency master sample (LF) and the high-frequency master sample (HF), defined by combining radio surveys and making cuts based on isolation and resolution. In Section 4 we describe how we selected two sub-samples of PS sources from the master samples based on the shape of their SEDs. An overview of each step in the sample selection is provided in Table 1, which includes the number of sources in our samples after each selection step.

3.1. Selecting the LoTSS+NVSS sample

We started the selection of the master samples with the LoTSS DR2 catalog. To ensure that source confusion did not impact the derived spectra, we made a selection based on whether the sources were isolated. Of all surveys used in this research, NVSS has the lowest resolution of 45''. Therefore we only selected sources in LoTSS that are isolated within 45''.

Deconvolution errors around very bright ($\gtrsim 200$ mJy) LoTSS sources can produce artifacts which can cause a source to appear as not isolated. In order to include these bright sources that are surrounded by complex noise structures, we included a source in the master sample if the neighboring source had a total flux density less than 10 % of the brightest source. The selection defined above contains 2,775,395 LoTSS sources that are isolated within 45''.

We expect all PS sources to be unresolved in LoTSS, since they generally are compact ($\lesssim 1''$, O'Dea 1998, Chhetri et al. 2018), and LoTSS has a resolution of 6''. Therefore, all unresolved sources in LoTSS were removed from the sample. We used the criterion for selecting resolved sources in LoTSS that

LoTSS+NVSS sample selection		
Step	Number of sources	
Total LoTSS catalogue		4,396,228
Isolated 45'' in LoTSS		2,775,395
Unresolved in LoTSS		2,586,267
S-code 'S' or 'M' in LoTSS		2,586,257
LoTSS+NVSS sample		146,975

LF sample selection		HF sample selection	
Step	Number of sources	Step	Number of sources
Total LoLSS catalog	42463	Total VLASS catalog	2,995,271
Isolated 45'' in LoLSS	40881	Recommended VLASS catalog	2,446,020
		Isolated 45'' in VLASS	1,384,792
		S-code 'S' or 'M' in VLASS	1,371,233
LF master sample	12,962	HF master sample	108,473
MPS sample	508	GPS sample	8,539

Table 1: A summary of the sample selection process. The number of sources in our sample that remain after each selection step is indicated.

was described by Shimwell et al. (2022). They defined an envelope that encompasses the 99.9 percentile of the R distribution, where $R = \ln(\frac{S_I}{S_P})$ contains the ratio between the integrated flux density S_I and the peak flux density S_P . A source is defined as being unresolved if R is larger than or equal to

$$R_{99.9} = 0.42 + \left(\frac{1.08}{1 + (\frac{S_{NR}}{96.57})^{2.49}} \right). \quad (1)$$

Here, the SNR is defined as $\frac{S_I}{\sigma_I}$, with σ_I the uncertainty on the integrated flux density. All sources with $R > R_{99.9}$ were deemed resolved, so we removed them from the sample. This step removed 6.8% of the sources in LoTSS, leaving us with 2,586,267 sources.

The above criterion has excluded the majority of the resolved sources, but it is based on the 99.9th percentile of the distribution. To remove resolved sources that might be left in the sample, we removed 10 sources with PyBDSF (Mohan & Rafferty 2015) S-code 'C' from our LoTSS selection, leaving 2,586,257 sources.

The isolated, unresolved sources in LoTSS were then cross-matched to NVSS, with a crossmatching radius of 10''. This number was selected to be slightly larger than the mean astrometric inaccuracy of NVSS (7''; Condon et al. 1998) because of we are limited by the sensitivity of NVSS in selecting GPS sources. The resulting LoTSS+NVSS sample contains 146,975 sources and forms the basis for both master samples defined in this work. Below, the LF and HF master samples are introduced separately.

3.2. Low-Frequency sample

To ensure we only consider a single source in NVSS, we demand all sources in LoLSS DR1 be isolated at 45'', with sources being ten times brighter than their neighbor being allowed in. This criterion removed 1,582 sources from the LoLSS sample, leaving us with 40,881 sources. We crossmatched the LoTSS+NVSS sample defined above to our selection of LoLSS, with a cross-matching radius of 5'', which produces our LF sample. This crossmatching radius was chosen in relation to the astrometric inaccuracy of LoLSS, where we take into account that we study

low SNR sources and therefore require a slightly larger cross-matching radius.

3.3. High-Frequency master sample

We defined the HF sample by crossmatching the LoTSS+NVSS sample to the VLASS QL component catalog. The entire VLASS QL epoch 2 catalog contains 2,995,271 components and still contains duplicates due to the overlap of the QL images. As recommended by the user guide (Gordon 2023), we selected only the sources without a duplicate, or sources with the best signal-to-noise ratio among multiple duplicate sources. We also select only sources with quality flags 0 or 4, according to their recommendations. This selection was designed to limit the contamination of spurious detections stemming from the limited quality of the QL images. After making these cuts to obtain reliable flux density measurements, we were left with a VLASS sample containing 2,446,020 components.

We also selected only sources in VLASS that are isolated in 45''. Sources with a neighbor within 45'', where the total flux density of this source is at least ten times brighter than their neighbor, were included in the sample since these neighbors are likely spuriously identified sources caused by sidelobe structures. By removing these clustered sources, we are left with 1,384,792 sources.

After removing the clustered sources, we also removed any source with a PyBDSF S-code 'C', which removed 13,559 sources from our sample, leaving us with only 'S' or 'M' S-code sources. Our final VLASS catalog contains 1,371,233 sources.

We then crossmatched this sample to the LoTSS+NVSS sample with a crossmatching radius of 2.5''. This crossmatching radius is slightly larger than the astrometric accuracy of VLASS (0.5 – 1''; Gordon 2023). VLASS is more sensitive to compact core components due to the lack of short baselines of the VLA, while LoTSS is more sensitive to extended lobe emission due to the abundance of short baselines of LOFAR. Furthermore, the core of a radio galaxy generally has a flatter spectrum than its lobes, causing the core to dominate over the lobes at higher frequencies. These effects might cause a shift in position larger than the astrometric inaccuracy, demanding a bigger crossmatching radius. We found 108,473 sources in this crossmatched sample, which we refer to as the HF master sample.

Though it was expected that approximately all sources in the LoTSS+NVSS sample have a match in VLASS, we found that only 73% of the sources in the LoTSS+NVSS do. If the isolation criterion was not applied, this number would be 86%. Thus 13% of the sources without a VLASS match are likely isolated and unresolved at 6'' in LoTSS, and resolved in VLASS at 2.5'', which causes them to be not isolated in VLASS, thus removed from the sample.

We account for the other 14% of sources in LoTSS+NVSS that do not have a VLASS detection via several other factors. We found that 0.4% of the sources in the LoTSS+NVSS sample have missing VLASS detections because of missing VLASS coverage. 3.6% of the LoTSS+NVSS sources are too faint to be detected in VLASS, or VLASS has high noise in that region of the sky.

For the remaining 10% of sources with a missing VLASS detection, we found they were marginally resolved in LoTSS at 6'' but passed our source size selection criterion. At the VLASS resolution of 2.5'', these sources are strongly resolved. In particular, VLASS is more sensitive to compact structures, while radio lobes tend to have steeper spectra than the core. Therefore VLASS has difficulty in detecting resolved lobes than LoTSS, and some of these sources are then resolved out.

We investigated how these resolved sources got incorrectly labeled as unresolved in our selection process. In the LoTSS images, these sources look like standard double-lobed radio sources in LoTSS, where the lobes get fit as 2 separate components by *PyBDSF*. These components are further apart than 47'', and they pass the unresolved criteria from Equation 1. We have thus confirmed that the majority of sources with missing VLASS detections are resolved in VLASS. This is not an issue for our science goal of identifying PS sources since the small angular sizes of almost all PS sources imply they are unresolved in VLASS.

3.4. Crossmatching to additional radio surveys

We crossmatched additional radio surveys to our LF and HF master samples, as well as the LoTSS and LoLSS inband spectra, using a crossmatching radius of 5''. The additional radio surveys are the TIFR GMRT Sky Survey Alternative Data Release 1 (TGSS; Intema et al. 2017) at 150 MHz, the Faint Images of the Radio Sky at Twenty-centimeters (FIRST; Becker et al. 1995) at 1.4 GHz, the Westerbork Northern Sky Survey (WENSS; Rengelink et al. 1997) at 326 MHz, and the Very Large Array Low-Frequency Sky Survey Redux (VLSSr; Lane et al. 2014) at 74 MHz. These surveys are not used for spectral index fitting but are used as visual guides in the SED plots.

4. Peaked-spectrum sources

From the LF and HF master samples, we identified PS sources from the shape of their SED. The SED between two flux density measurements can be described by a power law,

$$S = av^\alpha, \quad (2)$$

where α is the spectral index, and a is the normalization parameter. We use least-squares fitting to determine α and a .

In the LF master sample, we define α_{low} to be the spectral index between LoLSS and LoTSS, and α_{high} to be the spectral index between LoTSS and NVSS. In the HF master sample, we defined α_{low} to be the spectral index between LoTSS and NVSS, and α_{high} to be the spectral index between NVSS and VLASS.

Since we derive a and α from a fit to only two flux density measurements, the covariance matrix of the fit can not provide an uncertainty on the fit. To find the uncertainty σ of the spectral index, we use error-in-variables regression.

We defined a source to be PS if $\alpha_{\text{low}} > \sigma_{\alpha_{\text{low}}}$ and $\alpha_{\text{high}} < 0$. This criteria ensures that sources have a peak in their spectrum with at least a 1σ certainty for α_{low} . We are less strict for α_{high} , since any source with a positive α_{low} must have a turnover at higher frequencies. Then if $\alpha_{\text{high}} < 0$, we are sure that the turnover does not occur at higher frequencies than the upper survey frequency. By using the uncertainty in the lower spectral index we were sure to remove the majority of flat spectrum sources that might contaminate our sample.

4.1. Megahertz-peaked spectrum sample

We present the color-color plot for the LF sample in Figure 2. The lower right quadrant contains PS sources, plotted in red. In the LF master sample of 12,962 sources, we find 508 PS sources (3.9%), which we will refer to as the megahertz-peaked spectrum (MPS) sample. The MPS sample is the largest sample of MPS sources identified to date, 1.4 times larger than the sample by Slob et al. (2022). The MPS sources have a spectral peak approximately at 144 MHz, and are indicated in red in the color-color plot.

The method used so far for selecting the MPS sample is similar to that employed by Slob et al. (2022), where the main difference between our work and Slob et al. is that they used the LoLSS preliminary data release (PDR), while in this work we used Data Release 1 (DR1). DR1 is more sensitive and has a higher resolution (15'') than the PDR (47'') since direction-dependent effects have been corrected. We do not expect that the change of resolution has a significant effect on the classification of PS sources since the LoTSS+NVSS sample used in both of our works only includes isolated sources in 47''.

We compared the sample by Slob et al. to our MPS sample. One would expect to find that most, if not all, of the 373 PS sources in the sample by Slob et al. are also present in the sample of 728 MPS we would find. After accounting for sources that do not have a LoLSS observation in both the PDR and DR1, we find there are 148 sources that were identified as PS in the work by Slob et al., that are not identified as MPS sources in our work. Conversely, there are 70 sources that we identify as PS sources in our MPS sample, that were not identified in Slob et al. as PS sources.

We find that this discrepancy is caused by a significant inconsistency in the reported flux densities for individual sources between the PDR and DR1. This inconsistency causes α_{low} to be different for sources in our sample and in the sample by Slob et al. As was outlined by de Gasperin et al. (2023), the inconsistency can be explained by systematic effects dominating over the noise in the PDR. These effects cause the flux density of individual sources to vary significantly between the PDR and DR1, which causes sources to be mislabeled in the Slob et al. sample. The PDR should thus be used with care. We assume DR1 is more accurate and we will continue working with this survey in the rest of this work.

4.2. Gigahertz peaked-spectrum sample

In Figure 3 we plot the color-color plot for the HF master sample. We used the same selection criteria as for the MPS sample to define the gigahertz-peaked spectrum (GPS) sample. In

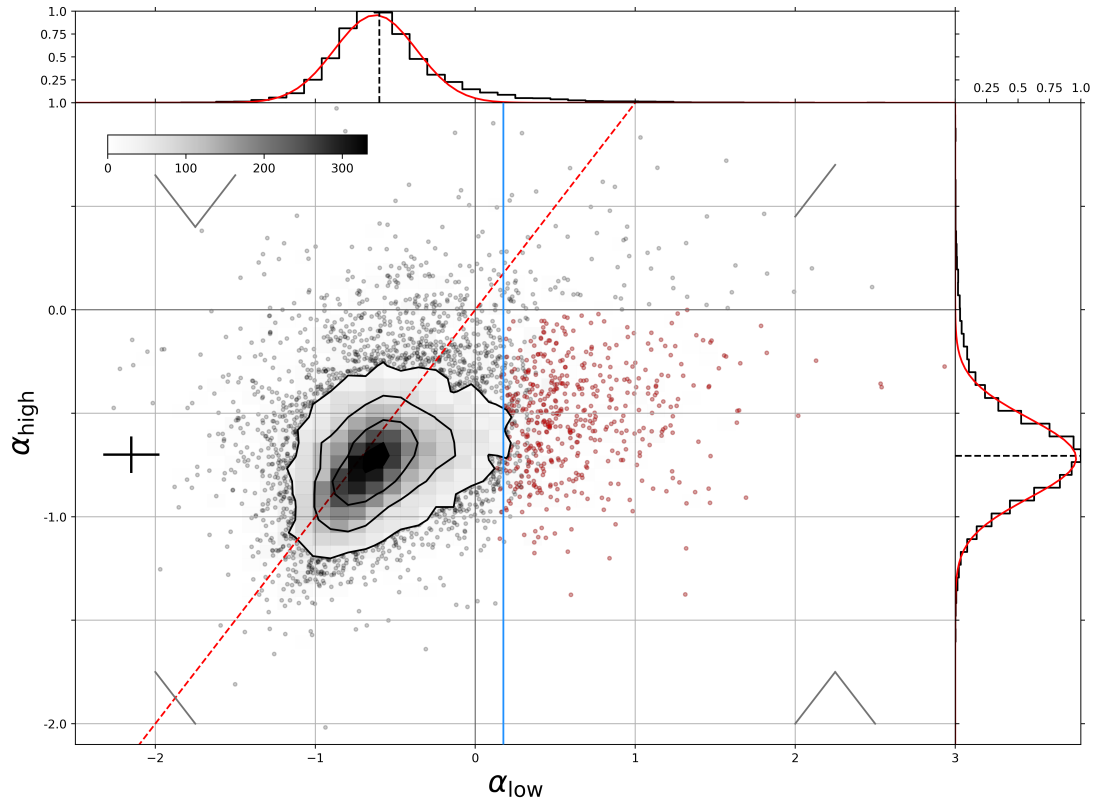


Fig. 2: Color-color plot for the 12,962 sources in our MPS sample, where α_{low} is the spectral index between LoLSS (54 MHz) and LoTSS(144 MHz), and α_{high} is the spectral index between LoTSS and NVSS(1400 MHz). PS sources exist in the lower right quadrant and are indicated by the red color. The blue line represents the median of the error of α_{low} . The contours represent 17, 60, 168, and 308 sources. It should be noted that there might be PS that are not indicated in red because they are hidden by the contours. The red dashed line represents the 1:1 ratio of the spectral indices. The median error bars are plotted instead of the individual errors, for readability. The normalized distributions of α_{low} and α_{high} are plotted, with a median and standard deviation of -0.6 ± 0.4 respectively -0.7 ± 0.2 . Mock SEDs are shown, to indicate the rough shape the SED of a source in each quadrant would have.

the HF master sample of 108,473 sources, we identified 8,539 GPS sources, which corresponds to 7.9 %. These sources peak around 1400 GHz, and are indicated in red. The GPS sample is the largest sample of PS sources to date, almost 6 times larger than the sample isolated by Callingham et al. (2017).

In this work, uncertainties are dominated by systematic uncertainties between surveys, rather than individual uncertainties on sources. Therefore, we assumed the uncertainty on flux measurements is always 10% of the flux density in LoTSS, NVSS, and VLASS, to account for the systematics between surveys. For sources in LoLSS, we are studying a lower SNR regime, so we used the reported flux density uncertainties for LoLSS. The precision of LoLSS is 6% (de Gasperin et al. 2023).

4.3. Comparison to literature PS samples

To confirm the validity of our selection process, we compared our MPS and GPS samples to previously identified CSS, GPS, CSO, and HFP samples (O'Dea 1998; Snellen et al. 1998, 2000; Peck & Taylor 2000b; Tinti et al. 2005; Labiano et al. 2007; Edwards & Tingay 2004; Randall et al. 2011).

45 of the literature sources were in our HF sample, 13 of which we identified as GPS sources. There are four reasons the remaining 32 were not identified as PS sources. Firstly, 13 of those sources are CSS sources, which do not have peaks in the frequency range of our surveys. Secondly, six sources had posi-

tive spectral indices over the whole frequency range of our surveys, indicating they have turnover at $\gtrsim 3$ GHz. Thirdly, seven sources had an uncertainty on α_{low} that was too large, which indicates that the spectral peak is abnormally broad or occurs near the low end of the frequency window. Finally, six sources showed significant variability in their SEDs, indicating they are likely blazars. In light of this, we conclude that our selection process is valid for our GPS sample. Of the literature PS sources, three were in our LF sample, which we did not identify as MPS sources. These three sources are also in the HF sample, therefore we will not discuss them separately here.

To highlight the diversity of PS sources we identified, we highlight the source B1315+415 in Figure 4. B1315+415 was identified as a PS source by Labiano et al. (2007), with a turnover at 2.3 GHz. The LoTSS image shows significant extended emission around a compact core. We interpret the combination of extended structure around a PS core as evidence this source has restarted activity.

4.4. Sources with extreme spectra

In our LF sample, we find three PS sources with $\alpha_{low} > 2.5$, and in the HF sample, we find one such source. These sources are interesting because such steep spectral indices below the peak imply that SSA can not be responsible for the turnover (O'Dea 1998). Therefore, such sources may be more consistent with the

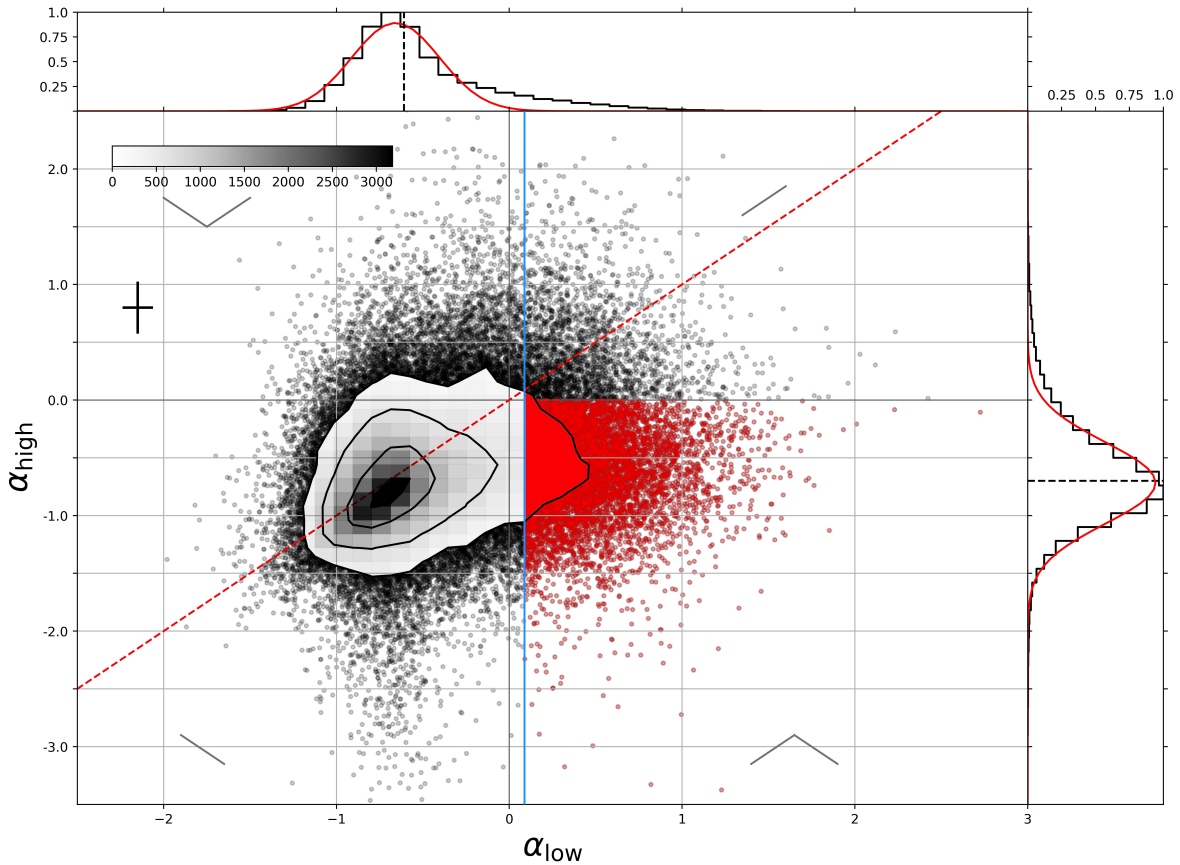


Fig. 3: Color-color plot for the 108,473 sources in our GPS sample, where α_{low} is the spectral index between LoTSS (144 MHz) and NVSS (1400 MHz), and α_{high} is the spectral index between NVSS and VLASS (3 GHz). PS sources exist in the lower right quadrant and are indicated in red. The blue line represents the median of the error of α_{low} , which corresponds to the median of the selection limit of PS sources. The contours represent 134, 416, 1349, and 2800 sources. It should be noted that there are also PS sources that are not indicated in red because they are hidden by the contours. The red dashed line represents the 1:1 ratio of the spectral indices. The median error bars are plotted instead of the individual errors, for readability. The normalized distributions of α_{low} and α_{high} are plotted, with a median and standard deviation of -0.6 ± 0.4 respectively -0.7 ± 0.5 . Mock SEDs are shown, to indicate the rough shape the SED of a source in each quadrant would have.

frustration hypothesis of PS sources. The SEDs of these extreme sources can be found in Figure 5. We indicate the exact spectral indices in the caption.

To all flux density measurements available for these sources, we fit:

$$S(\nu) = \frac{S_{peak}}{(1 - e^{-1})} \cdot \left(\frac{\nu}{\nu_{peak}}\right)^{\alpha_{thick}} \cdot (1 - \exp(-\nu/\nu_{peak}))^{(\alpha_{thin} - \alpha_{thick})}, \quad (3)$$

where α_{thin} and α_{thick} indicate the spectral indices in the optically thin and optically thick regions of the SED, respectively, and ν_{peak} indicates the peak frequency.

We want to particularly highlight 87GB B0903+6656 as its measurement of $\alpha_{low} > 2.5$ is robust. Previously, the source has been identified as a flat-spectrum radio source by Healey et al. (2007). The extreme turnover is consistent with a non-detection of the source at 408 MHz (Marecki et al. 1999). The host of this source has been identified as a quasar by e.g. Souchay et al. (2009). Followup HI absorption or X-ray observations are warranted to confirm if the inferred dense circumnuclear medium surrounds the core-jet structure of the source.

4.5. Other sources with interesting spectra

We note that the upper right quadrant of the color-color plots contains sources with a positive spectral index across the entire frequency range probed by our surveys, therefore a spectral turnover must occur at some frequency higher than our observing window. There are 95 sources in the upper right quadrant of Figure 2 of the LF sample. These sources are likely either GPS or HFP sources, peaking above ~ 1.4 GHz. Similarly, the upper right quadrant of Figure 3 of the HF sample contains 3015 sources, which are most likely HFP sources as they must peak above ~ 2 GHz. Out of the 95 sources in the upper right quadrant of the LF sample, 54 are indeed classified as GPS sources in our sample.

Sources in the upper left quadrants of the color-color plots exhibit a convex spectrum, which is likely indicative of multiple epochs of AGN radio activity (Callingham et al. 2017). The SED of a source that shows that convex spectrum is presented in Figure 6. Such sources are composite sources, with a steep-spectrum power-law component at low frequencies and an inverted component at high frequencies. In the LF sample, there are 134 convex spectrum sources, and in the HF sample there are 5610. Follow-up observations at higher frequencies ($\gtrsim 5$ GHz)

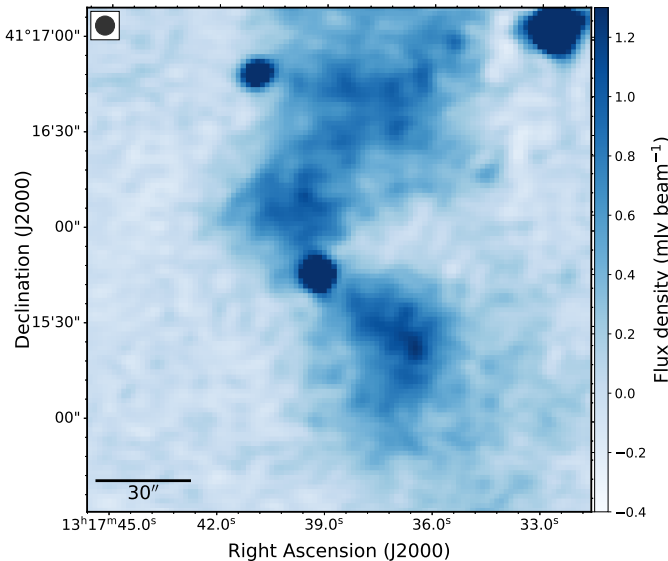


Fig. 4: The LoTSS view of B1315+415, which is likely a restarted PS source. The LoTSS beam size is indicated in the upper left corner, and the color bar indicates the flux density per beam. **This plot likely will have an inset of the SED, did not have time before draft version**

are required to trace the higher frequency turnover and ensure the spectrum is not a product of intrinsic variability.

To the SED in 6 we fit equation 3, with an additional power law term added to constrain the upturn. This source, NGC 3894, was identified as a nearby low-power CSO by Peck & Taylor (2000a); Taylor et al. (1998). Tremblay et al. (2016) use Very Long Baseline Interferometry (VLBI) and find this source has a flat-spectrum core with diffuse lobes extending to the northwest and southeast. They find the core has a strongly inverted spectral index ($\alpha \sim 1 - 1.5$) between 5 and 8 GHz.

5. Euclidean normalized source counts

We studied the evolution of the PS sources in our samples via the 144 MHz and 1400 MHz differential source counts for the MPS and GPS samples, respectively. If PS sources are indeed young radio galaxies, we would expect an offset between the source counts of a complete sample of radio-loud AGN and the source counts of our samples of PS sources. Such an offset would correspond to the difference in lifetimes and cosmological evolution for the different types of sources.

5.1. MPS sample source counts

To compute the 144 MHz source counts for the MPS sample, we only included sources with LoTSS flux densities above $S_{144\text{MHz}} > 18$ mJy. This limit corresponds to the 95 % completeness limit of LoLSS of $S_{54\text{MHz}} = 11$ mJy (de Gasperin et al. 2021), rescaled to 144 MHz assuming a power law with a spectral index of 0.52. The spectral index of 0.52 is the median of α_{low} in the MPS sample.

There are 503 MPS sources with a 144 MHz flux density brighter than 18 mJy. The resulting normalized source counts can be found in Table A.1 and in Figure 7. We removed the lowest flux density bin, as it was severely impacted by incompleteness.

To validate our sample selection methods, we compare our source counts with source counts from samples of PS sources from the literature. We plot the 144 MHz source counts of the MPS sample as obtained by Slob et al. (2022) and find they coincide with our measurements. We also plot the source counts from the PS sample of Callingham et al. (2017). Only sources with flux density $S_{143\text{MHz}} > 1$ Jy were included, which corresponds to the reported 100 % flux density completeness of the GLEAM survey. These source counts, though not extending to the same sensitivity, do correspond well to the source counts we find for our sample in the higher signal-to-noise regime.

In order to compare the populations of PS sources with a general population of radio sources, we also consider the source counts from the LoTSS Deep field (Mandal et al. 2021), which are the deepest 150 MHz source counts published to date. We find that the source counts of our MPS sample, as well as the other literary PS samples plotted, have a significant offset from the source counts of the AGN sample, while the shape of the distribution remains similar. This offset, with no shift in its peak, might indicate that MPS sources are indeed the young progenitors of FR I and FR II sources, with shorter lifetimes.

We use orthogonal distance regression (ODR) to fit the 144 MHz Massardi et al. (2010) model, divided by a scaling parameter, to the source counts of our MPS sample. We find that the MPS sample has a best-fitting scaling parameter of 45 ± 2 , which would indicate that MPS sources are roughly 45 times less abundant than AGN at 144 MHz. We plot the χ^2 residuals between our MPS source counts and the best fit for the scaled model in the bottom plot of Figure 7.

5.2. GPS sample source counts

We computed the 1400 MHz source counts for our GPS sample, which is limited by the completeness of NVSS, which is 95% complete at $S_{1400\text{MHz}} = 3.24$ mJy (Condon et al. 1998). We only included sources with NVSS flux density above this completeness limit. There are 7174 sources in the GPS sample above the completeness limit, which we used to make the source counts.

The Euclidean normalized source counts at 1400 MHz can be found in Table A.1 and in Figure 8. In this figure, we also plot the source counts for the sample of PS sources from Snellen et al. (1998). These source counts were evaluated at the individual peak frequencies for each PS source, corresponding to a median frequency of 2 GHz. We rescaled these source counts to 1400 MHz assuming the power law from Equation 2 with a spectral index of -0.8 .

In order to compare the source counts of our GPS sources with a general population of AGN, we consider the 1400 MHz model from Massardi et al. (2010), which was constructed using data presented by Zotti et al. (2009).

We again find our GPS samples have a significant offset from the AGN sample, while the shape of the distribution remains similar. The offset can indicate the relative lifetimes of GPS sources. Through ODR fitting we find that the source counts of the GPS sample are scaled down by a factor 29 ± 1 compared to the AGN source counts. We can thus conclude that GPS sources are roughly 29 times less abundant than radio AGN at 1400 MHz.

6. Discussion

We determine the abundance of MPS and GPS sources in the radio sky using the source counts and their offsets we calculated in

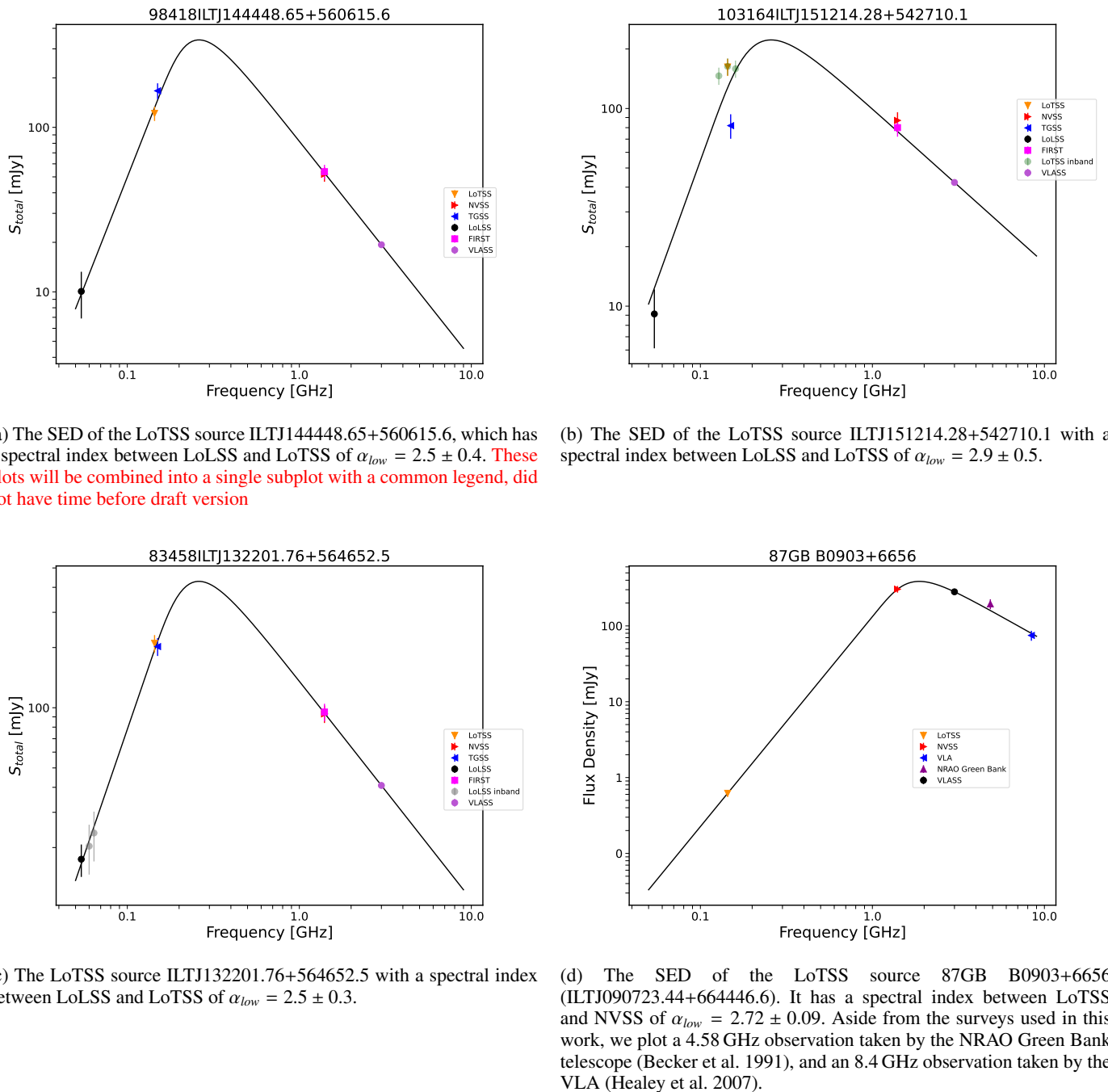


Fig. 5: The SEDs of the four sources in our sample with extremely steep spectral indices. The curve from Equation 3 was fitted to all radio flux density measurements available for these sources and is indicated as a dotted curve. The power laws fitted are also indicated.

Section 5. We find that $2.2 \pm 0.1\%$ of the radio source population at 144 MHz are MPS sources, and $3.3 \pm 0.1\%$ of the radio source population at 1400 MHz are GPS sources.

Slob et al. (2022) computed the radio source counts of their MPS sample, and found they were scaled down by a factor of 40 compared to a general sample of radio-loud active galactic nuclei (AGN). This number indicates that 2.4% of the radio sky at 144 MHz consists of MPS sources, similar to the number we find. Callingham et al. (2017) find that $\sim 4.5\%$ of the radio source population is a PS source between 72 MHz and 1.4 GHz,

which roughly corresponds to the combined frequency window of our MPS and GPS samples. Conversely, O'Dea (1998) indicates that $\approx 10\%$ of the bright radio sky are GPS sources, which is 3 times more than the percentage we find. Snellen et al. (1998) report an offset of approximately 250 between the source counts of typical large-scale radio sources and the source counts of their GPS sample. This number would indicate that 0.4% of the sources in the radio sky at 2 GHz are GPS sources, 8 times lower than we report. Therefore, we find that the abundances of GPS sources as reported by Snellen et al. (1998) and O'Dea

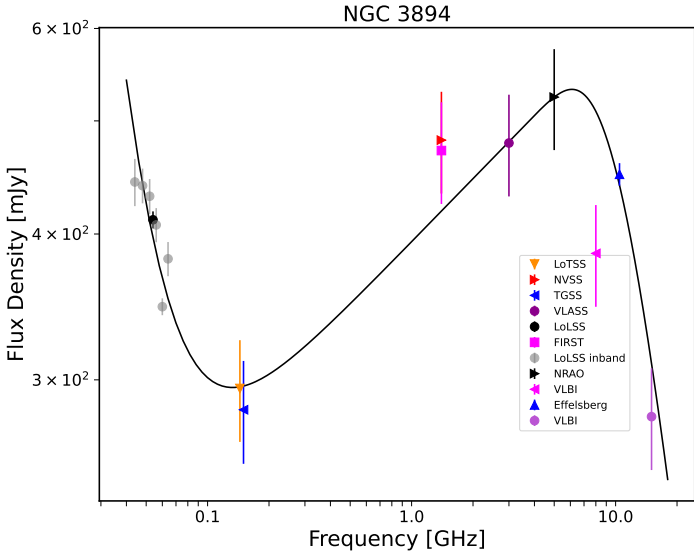


Fig. 6: The convex SED of NGC 3894 (ILTJ114850.36+592456.2). Additional high-frequency measurements were added, a 5 GHz NRAO 300-ft telescope measurement (Sramek 1975), a 10.45GHz 100m Effelsberg telescope measurement (Pasetto et al. 2016), and two VLBI measurements at 8 GHz and 415 GHz by Tremblay et al. (2016).
I will see if I can add some more photometry measurements, and make the colors and symbols consistent with other plots

(1998) vary by a factor of roughly 25 of each other. The Snellen source counts offsets were calculated by rescaling the 325 MHz radio source counts from the WENSS mini-survey region Rengelink et al. (1997) to 2 GHz using a spectral index of -0.85 . Since Snellen et al. (1998) published, sensitive source counts at frequencies closer to 2 GHz have become available, therefore we calculate the offset of the Snellen et al. (1998) GPS source counts, rescaled to 1400 MHz with a spectral index of -0.8 , to the 1400 MHz model by Massardi et al. (2010). We find an offset of 51 ± 20 , which is 5 times lower than what Snellen et al. (1998), originally reported, and corresponds to a GPS abundance of $1.9 \pm 0.7\%$ of the radio sky at 2 GHz, which is closer to the value we report.

If we assume all PS sources evolve into FRI and FRII radio sources and there is no cosmological evolution, the source count offset captures the difference in lifetimes between PS sources and large-scale radio sources. We then find that MPS sources have lifetimes roughly 44 times less than large-scale radio AGN, and GPS sources have lifetimes roughly 29 times shorter than AGN. We also find that MPS sources have lifetimes 1.6 times less than GPS sources.

To explain the different relative lifetimes with the youth hypothesis, we need to understand the physical circumstances and formation of young AGN. Three-dimensional simulations by Sutherland & Bicknell (2007) demonstrated the interaction of a light hypersonic jet with an inhomogeneous thermal and turbulently supported disk in an elliptical galaxy. While the source was smaller than 1 kpc, coinciding with the GPS phase (O'Dea 1998), it was still an energy-driven bubble. As the source gets larger, coinciding with the MPS phase, jets break out and classical radio lobes start to form. We conclude that the GPS phase occurs when the jets are traveling quite slowly and constantly

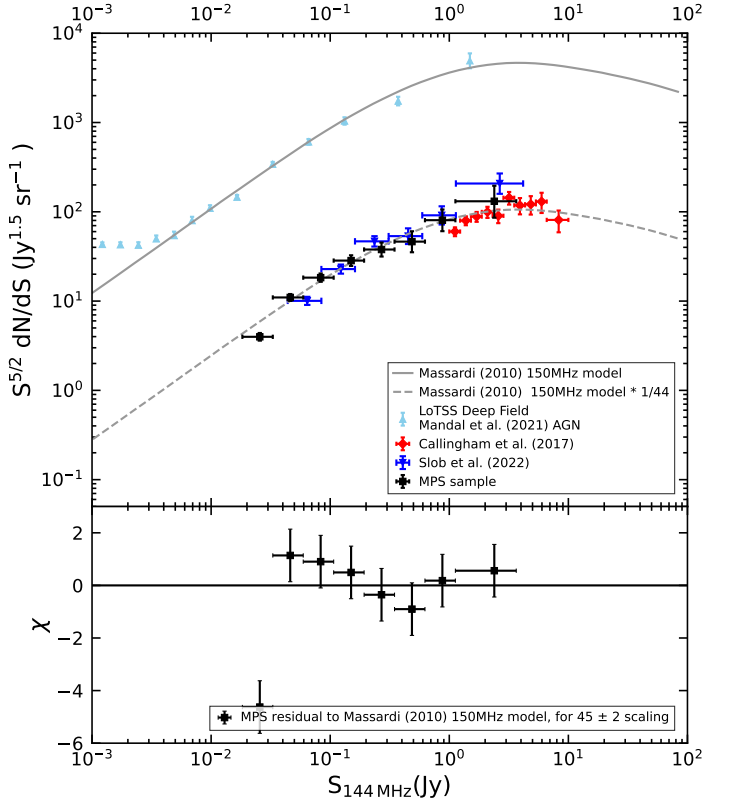


Fig. 7: The top panel shows the 144 MHz Euclidean normalized differential source counts of our MPS sample. Plotted are also the source counts from Callingham et al. (2017) and Slob et al. (2022), which are samples of PS sources. To compare them to a general population of AGN, the 150 MHz source counts from the LoTSS Deep Field (Mandal et al. 2021) are plotted. The 150 MHz model from Massardi et al. (2010) is indicated by the solid gray line. This same model scaled down by a factor of 44 is indicated by the dashed gray line. In the bottom panel, we plot the residuals of our MPS source counts to the Massardi et al. (2010) 150 MHz model rescaled by a factor 45.

through the bubble, but for the MPS phase the jets have already escaped the bubble and are growing faster than previous phases. This change in propagation speed could explain why we find that GPS sources live longer than MPS sources.

It should be noted that the definitions of the different classes of PS sources are not based on any physical parameters, but rather on observational limits. The frequency windows that define when a source is an MPS source or a GPS source have arbitrary boundaries. Therefore, a comparison between samples has to be done with care, ideally covering the same fractional bandwidth when selecting PS sources.

Note that our inference about the lifetime of PS sources from source counts ignores cosmological evolution. What is required is to construct luminosity functions of our MPS and GPS, as it would allow us to calculate relative abundances of MPS and GPS sources as a function of redshift. Slob et al. (2022) have computed luminosity functions for their sample of MPS sources, and found that there is no cosmological evolution between redshifts 0.1 and 0.3. Therefore the source counts capture the lifetimes sufficiently well.

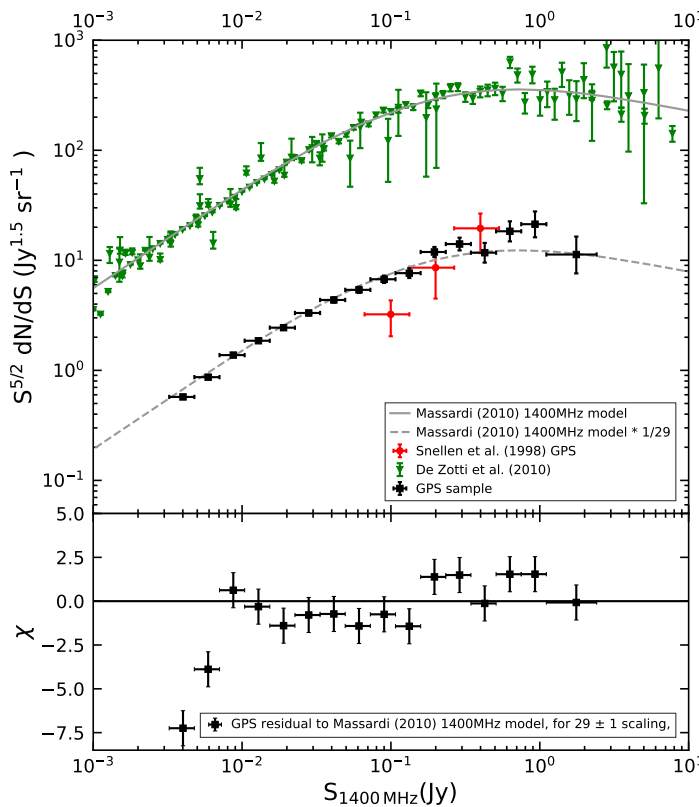


Fig. 8: The top panel shows the 1400 MHz Euclidean normalized differential source counts of our GPS sample. Plotted are also the source counts of the PS sample from Snellen et al. (1998). To compare our source counts to those of a general population of AGN, the 1400 MHz source counts from Zotti et al. (2009) are plotted. The 1400 MHz model from Massardi et al. (2010) is indicated by the solid gray line. This same model scaled down by a factor of 30 is indicated by the dashed gray line. In the bottom panel, we plot the residuals of our GPS source counts to the Massardi et al. (2010) 1400 MHz model rescaled by a factor 29.

7. Conclusions

The recent revolution in wide-field radio surveys, both in sensitivity, sky area, resolution, and frequency range, has made the study of statistical samples of PS sources possible for the first time. These samples allow us to study the abundance of GPS and MPS sources in the radio sky more accurately than ever before and allow us to draw conclusions about their relative lifetimes. In this work, we present a sample of 8,539 GPS sources with spectral turnovers near 1400 MHz, and a sample of 508 MPS sources with turnovers near 144 MHz. These samples have been selected using LoTSS, LoLSS, NVSS, and VLASS. Our MPS sample is 1.4 times larger than the previously known largest sample of PS sources in the same frequency range as constructed by Slob et al. (2022). Our GPS sample is almost six times larger than the previously known largest sample of PS sources (Callingham et al. 2017).

These samples of PS sources were defined from two master samples, consisting of unresolved and isolated radio sources with no assumption about their spectral shape. From our LF master sample, we classified sources as MPS sources if the power law spectral index between LoLSS and LoTSS is positive, and the spectral index between LoTSS and NVSS is negative. Sim-

ilarly for the HF sample, a source is considered a PS source if the spectral index between LoTSS and NVSS is positive, and the spectral index between NVSS and VLASS is negative. This criteria selects sources with a concave SED. 3.9% of the sources in our LF sample were identified as MPS sources, and 7.9% of the sources in our HF sample were identified as GPS sources. We find the following:

- We were able to identify four PS sources with a lower spectral index of > 2.5 , the limit that SSA can produce. These sources must thus have spectral turnovers associated with FFA, indicating that these sources are likely associated with a dense circumnuclear environment.
- We identified B1315+415 as a possible restarted PS source since it has extended lobes and a compact core, and the SED of this source shows a spectral turnover.
- We calculated the 144 MHz respectively 1400 MHz Euclidean normalized source counts for our MPS and GPS samples and found that their shapes match those of the source counts of large-scale AGN, scaled down by a factor 45 ± 2 for the MPS sample and a factor 29 ± 1 for the GPS sample. From this offset, we find that $2.2 \pm 0.1\%$ of the radio source population at 144 MHz are MPS sources, and $3.3 \pm 0.1\%$ of the radio source population at 1400 MHz are GPS sources.
- If we interpret these offsets at face value, they imply that MPS sources live roughly 44 times shorter than large-scale AGN, and GPS sources live roughly 29 times shorter. They also imply that GPS sources live roughly 1.6 times longer than MPS sources. It should be noted that we are unable to identify GPS sources with a spectral turnover at higher frequencies than 2 GHz, while the literature defines GPS sources as sources with a turnover up until approximately ~ 5 GHz. Therefore we are likely missing a large fraction of GPS sources. However, the definitions of the different categories of PS sources are based on arbitrary parameters, therefore our conclusions hold for the frequency windows we define.

The conclusions we draw from the source counts should be interpreted carefully, as they do not account for any redshift evolution. Using luminosity functions, we would be able to study the evolution of the abundance of PS sources as a function of redshift. Once such luminosity functions are constructed, modeling them could help us understand the slope of the luminosity functions. We then have a better understanding of how the number density of PS sources evolves with redshift, which helps us understand the evolution between MPS and GPS sources.

Since we only used three flux density measurements to determine and classify the SEDs of our sources, we were limited in determining their exact turnover frequency. Spectral index fitting on more than three flux density measurements would allow us to determine the turnover frequency more precisely, which could help us determine the linear sizes of these sources according to the relation between linear size and turnover frequency by O'Dea (1998). We could then plot these sources in a diagram of, for example, linear size against radio power, for the sources with available redshift. Such a diagram provides a snapshot of radio source evolution, where individual sources will trace out trajectories on the plane. Comparing our MPS and GPS samples on this plane will be valuable to further study the evolution between these types of sources.

We have shown that the improvement in sensitivity of wide-field radio surveys in the past few decades allows us for the first time to make robust statements about the relative abundances of

MPS and GPS sources. After completion of the radio surveys used in this work, we can expect an even further increase in PS sample size. The size of our GPS sample is limited by the survey area of LoTSS, which has currently covered 27% of the northern sky (Shimwell et al. 2022). Upon completion of LoTSS, we thus expect to find $\sim 32 \cdot 10^3$ GPS sources. The MPS and LF samples are limited by the LoLSS sky area, which will also eventually cover the entire northern sky. Currently, 650 degree 2 has been observed (de Gasperin et al. 2023), which is only $\sim 3\%$ of the northern sky. We would then expect to find $sim17 \cdot 10^3$ MPS sources once both LoLSS and LoTSS have been completed.

Aside from the completion of radio surveys already being made, new radio telescopes that will be built in the coming years promise an even greater sensitivity and resolution. LOFAR is a pathfinder for the Square Kilometer Array (SKA), which is a radio telescope currently being built in Australia and South Africa. SKA's low-frequency array will be eight times more sensitive and will have a 135 times faster survey speed than LOFAR, which is currently the most sensitive radio telescope in the low-frequency range. SKA's mid-frequency array will be almost five times more sensitive than the VLA (SKAO 2022). SKA will provide opportunities for studying larger and more sensitive samples of PS sources than ever before.

Acknowledgements. LOFAR data products were provided by the LOFAR Surveys Key Science project (LSKSP; <https://lofar-surveys.org/>) and were derived from observations with the International LOFAR Telescope (ILT). LOFAR van Haarlem et al. (2013) is the Low Frequency Array designed and constructed by ASTRON. It has observing, data processing, and data storage facilities in several countries, which are owned by various parties (each with their own funding sources), and which are collectively operated by the ILT foundation under a joint scientific policy. The efforts of the LSKSP have benefited from funding from the European Research Council, NOVA, NWO, CNRS-INSU, the SURF Co-operative, the UK Science and Technology Funding Council and the Jülich Supercomputing Centre. The National Radio Astronomy Observatory is a facility of the National Science Foundation operated under cooperative agreement by Associated Universities, Inc. This research used the facilities of the Canadian Astronomy Data Centre operated by the National Research Council of Canada with the support of the Canadian Space Agency. This research has made use of "Aladin sky atlas" developed at CDS, Strasbourg Observatory, France, and of the NASA/IPAC Extragalactic Database (NED) operated by the Jet Propulsion Laboratory, California Institute of Technology, under contract with the National Aeronautics and Space Administration. Furthermore, this research has made use of NASA's Astrophysics Data System Bibliographic Services. This research has made use of the SIMBAD database, operated at CDS, Strasbourg, France. This research also made use of TOPCAT, an interactive graphical viewer and editor for tabular data (Taylor 2005). This research made use of APLpy, an open-source plotting package for Python Robitaille & Bressert (2012), Astropy, a community-developed core Python package for Astronomy (Astropy Collaboration et al. 2018), and of matplotlib, a Python library for publication quality graphics (Hunter 2007). This research made use of NumPy (Harris et al. 2020), and of SciPy (Virtanen et al. 2020).

References

- An, T. & Baan, W. A. 2012, The Astrophysical Journal, 760, 77
- Astropy Collaboration, Price-Whelan, A. M., Sipőcz, B. M., et al. 2018, AJ, 156, 123
- Baum, S. A., O'Dea, C. P., Murphy, D. W., & de Bruyn, A. G. 1990, A&A, 232, 19
- Becker, R. H., White, R. L., & Edwards, A. L. 1991, ApJS, 75, 1
- Becker, R. H., White, R. L., & Helfand, D. J. 1995, The Astrophysical Journal, 450, 559
- Bicknell, G. V., Dopita, M. A., & O'Dea, C. P. O. 1997, ApJ, 485, 112
- Callingham, J. R., Ekers, R. D., Gaensler, B. M., et al. 2017, The Astrophysical Journal
- Callingham, J. R., Gaensler, B. M., Ekers, R. D., et al. 2015, The Astrophysical Journal, 809, 168
- Carvalho, J. C. 1985, MNRAS, 215, 463
- Chhetri, R., Morgan, J., Ekers, R. D., et al. 2018, MNRAS, 474, 4937
- Condon, J. J., Cotton, W. D., Greisen, E. W., et al. 1998, The Astronomical Journal, 115, 1693
- Dallacasa, D., Stanghellini, C., Centonza, M., & Fanti, R. 2001, Astronomy and Astrophysics, 363
- de Gasperin, F., Edler, H. W., Williams, W. L., et al. 2023, The LOFAR LBA Sky Survey II. First data release
- de Gasperin, F., Williams, W. L., Best, P., et al. 2021, Astronomy & Astrophysics, 648, A104
- de Vries, N., Snellen, I. A. G., Schilizzi, R. T., & Mack, K. H. 2009, Astronomische Nachrichten, 330, 214
- Edwards, P. G. & Tingay, S. J. 2004, A&A, 424, 91
- Fanti, R., Fanti, C., Schilizzi, R. T., et al. 1990, A&A, 231, 333
- Gopal-Krishna, Patnaik, A. R., & Steppe, H. 1983, A&A, 123, 107
- Gordon, Y. 2023, CIRADA: VLASS Catalog User Guide
- Hale, C. L., McConnell, D., Thomson, A. J. M., et al. 2021, Publications of the Astronomical Society of Australia, 38
- Hales, S. E. G., Riley, J. M., Waldram, E. M., Warner, P. J., & Baldwin, J. E. 2007, Monthly Notices of the Royal Astronomical Society, 382, 1639
- Harris, C. R., Millman, K. J., van der Walt, S. J., et al. 2020, Nature, 585, 357
- Healey, S. E., Romani, R. W., Taylor, G. B., et al. 2007, ApJS, 171, 61
- Hill, G. J., Gebhardt, K., Komatsu, E., et al. 2008, Panor. Views Galaxy Form. Evol., 399, 115
- Hinshaw, G., Larson, D., Komatsu, E., et al. 2013, The Astrophysical Journal Supplement Series, 208, 19
- Hunter, J. D. 2007, Computing In Science & Engineering, 9, 90
- Intema, H. T., Jagannathan, P., Mooley, K. P., & Frail, D. A. 2017, Astronomy & Astrophysics, 598, A78
- Kaiser, C. R. & Best, P. N. 2007, Monthly Notices of the Royal Astronomical Society, 381, 1548
- Kunert-Bajraszewska, M., Gawroński, M. P., Labiano, A., & Siemiginowska, A. 2010, Monthly Notices of the Royal Astronomical Society, 408, 2261
- Labiano, A., Barthel, P. D., O'Dea, C. P., et al. 2007, A&A, 463, 97
- Lacy, M., Baum, S. A., Chandler, C. J., et al. 2020, Publications of the Astronomical Society of the Pacific, 132, 035001
- Lane, W. M., Cotton, W. D., van Velzen, S., et al. 2014, Monthly Notices of the Royal Astronomical Society, 440, 327
- Mandal, S., Prandoni, I., Hardcastle, M. J., et al. 2021, Astronomy & Astrophysics, 648, A5
- Marecki, A., Falcke, H., Niezgoda, J., Garrington, S. T., & Patnaik, A. R. 1999, A&AS, 135, 273
- Massardi, M., Bonaldi, A., Negrello, M., et al. 2010, Monthly Notices of the Royal Astronomical Society
- Mauch, T., Murphy, T., Buttery, H. J., et al. 2003, Monthly Notices of the Royal Astronomical Society, 342, 1117
- Mohan, N. & Rafferty, D. 2015, PyBDSF: Python Blob Detection and Source Finder, Astrophysics Source Code Library, record ascl:1502.007
- Murphy, T., Sadler, E. M., Ekers, R. D., et al. 2010, Monthly Notices of the Royal Astronomical Society, 402, 2403
- O'Dea, C. P. 1998, Publications of the Astronomical Society of the Pacific, 110, 493
- O'Dea, C. P. & Saikia, D. J. 2021, The Astronomy and Astrophysics Review, 29
- Owsianik, I. & Conway, J. E. 1998, A&A, 337, 69
- Pasetto, A., Kraus, A., Mack, K.-H., Bruni, G., & Carrasco-González, C. 2016, A&A, 586, A117
- Peck, A. & Taylor, G. B. 2000a, in EVN Symposium 2000, Proceedings of the 5th european VLBI Network Symposium, ed. J. E. Conway, A. G. Polatidis, R. S. Booth, & Y. M. Pihlström, 119
- Peck, A. B. & Taylor, G. B. 2000b, ApJ, 534, 90
- Peck, L. 1999, in Society of Photo-Optical Instrumentation Engineers (SPIE) Conference Series, Vol. 3713, Unattended Ground Sensor Technologies and Applications, ed. E. M. Carapezza, D. B. Law, & K. T. Stalker, 188–196
- Randall, K. E., Hopkins, A. M., Norris, R. P., & Edwards, P. G. 2011, MNRAS, 416, 1135
- Rengelink, R. B., Tang, Y., de Bruyn, A. G., et al. 1997, Astronomy and Astrophysics Supplement Series, 124, 259
- Robitaille, T. & Bressert, E. 2012, APLpy: Astronomical Plotting Library in Python, Astrophysics Source Code Library, record ascl:1208.017
- Shimwell, T. W., Hardcastle, M. J., Tasse, C., et al. 2022, Astronomy & Astrophysics, 659, A1
- SKAO. 2022
- Slob, M. M., Callingham, J. R., Röttgering, H. J. A., et al. 2022, Astronomy & Astrophysics, 668, A186
- Snellen, I. A., Schilizzi, R. T., de Bruyn, A. G., et al. 1998, Astronomy and Astrophysics Supplement Series, 131, 435
- Snellen, I. A. G., Schilizzi, R. T., Miley, G. K., et al. 2000, Monthly Notices of the Royal Astronomical Society, 319, 445
- Sobolewska, M., Siemiginowska, A., Guainazzi, M., et al. 2019, ApJ, 871, 71
- Souchay, J., Andrei, A. H., Barache, C., et al. 2009, A&A, 494, 799
- Sramek, R. 1975, AJ, 80, 771
- Stanghellini, C., Baum, S. A., O'Dea, C. P., & Morris, G. B. 1990, A&A, 233, 379

- Sutherland, R. S. & Bicknell, G. V. 2007, ApJS, 173, 37
Taylor, G. B., Wrobel, J. M., & Vermeulen, R. C. 1998, ApJ, 498, 619
Taylor, M. B. 2005, in Astronomical Society of the Pacific Conference Series, Vol. 347, Astronomical Data Analysis Software and Systems XIV, ed. P. Shopbell, M. Britton, & R. Ebert, 29
Tinti, S., Dallacasa, D., de Zotti, G., Celotti, A., & Stanghellini, C. 2005, A&A, 432, 31
Tremblay, S. E., Taylor, G. B., Ortiz, A. A., et al. 2016, MNRAS, 459, 820
van Breugel, W., Miley, G., & Heckman, T. 1984, AJ, 89, 5
van Haarlem, M. P., Wise, M. W., Gunst, A. W., et al. 2013, Astronomy & Astrophysics, 556, A2
Virtanen, P., Gommers, R., Oliphant, T. E., et al. 2020, Nature Methods, 17, 261
Wayth, R. B., Lenc, E., Bell, M. E., et al. 2015, PASA, 32, e025
Wilkinson, P. N., Booth, R. S., Cornwell, T. J., & Clark, R. R. 1984, Nature, 308, 619
Zotti, G. D., Massardi, M., Negrello, M., & Wall, J. 2009, The Astronomy and Astrophysics Review, 18, 1

Appendix A: Source counts

MPS sample

$\langle S \rangle_{\text{144 MHz}} [\text{Jy}]$	N_S	$S^{5/2} dN/ds_{-\sigma}^{+\sigma} [\text{Jy}^{1.5}/\text{sr}]$
0.035	138	$7.44^{+0.69}_{-0.63}$
0.066	121	$14.26^{+1.42}_{-1.29}$
0.123	74	$22.79^{+2.87}_{-2.64}$
0.229	47	$32.98^{+5.54}_{-4.79}$
0.429	25	$51.91^{+12.59}_{-10.3}$
0.801	17	$85.53^{+26.16}_{-20.52}$
2.347	8	$127.1^{+62.38}_{-43.91}$

GPS sample

$\langle S \rangle_{\text{1400 MHz}} [\text{Jy}]$	N_S	$S^{5/2} dN/ds_{-\sigma}^{+\sigma} [\text{Jy}^{1.5}/\text{sr}]$
0.004	1571	$0.57^{+0.01}_{-0.01}$
0.006	1320	$0.87^{+0.02}_{-0.02}$
0.009	1143	$1.38^{+0.04}_{-0.04}$
0.013	885	$1.86^{+0.06}_{-0.06}$
0.019	640	$2.44^{+0.1}_{-0.1}$
0.028	488	$3.32^{+0.16}_{-0.15}$
0.041	354	$4.36^{+0.24}_{-0.23}$
0.061	250	$5.39^{+0.36}_{-0.34}$
0.09	176	$6.73^{+0.55}_{-0.51}$
0.133	105	$7.65^{+0.82}_{-0.75}$
0.196	98	$11.9^{+1.33}_{-1.2}$
0.289	63	$14.06^{+2.0}_{-1.77}$
0.427	28	$11.73^{+2.66}_{-2.2}$
0.63	27	$18.36^{+4.25}_{-3.51}$
0.929	17	$21.3^{+6.31}_{-5.11}$
1.759	9	$11.29^{+5.15}_{-3.69}$

Table A.1: The 144 MHz respectively 1400MHz source counts for our MPS and GPS samples. $\langle S \rangle$ is the central flux density of every flux bin in Jy, N_S is the number of sources in each bin, and $N_{-\sigma}^{+\sigma}$ are the normalized differential source counts in $[\text{Jy}^{1.5}/\text{sr}]$.